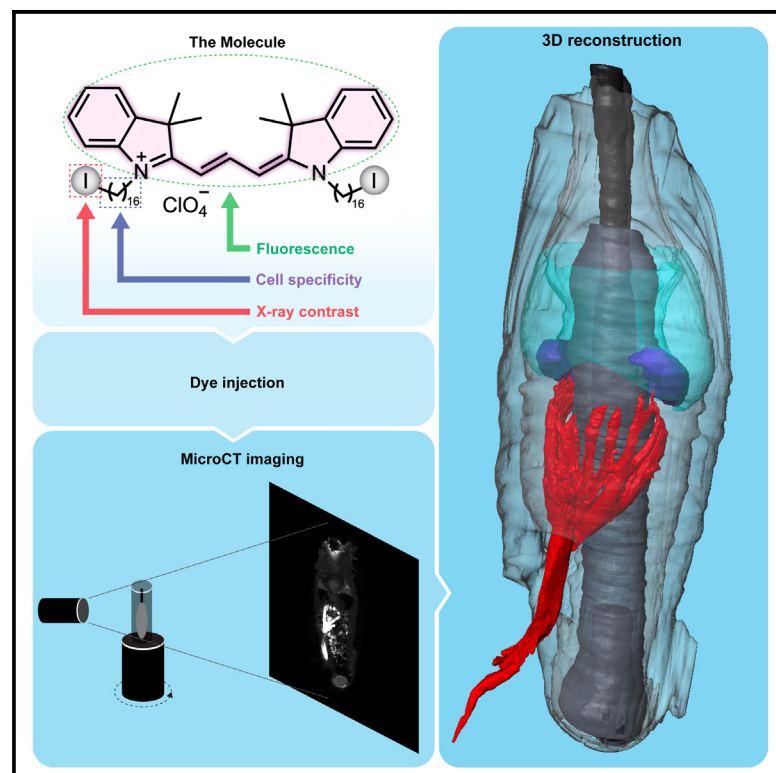**Article**

DiI-CT—A bimodal neural tracer for X-ray and fluorescence imaging

Graphical abstract

Authors
Ben Gerhardt, Kristin Klaue,
Lennart Eigen, Jutta Schwarz,
Stefan Hecht, Michael Brecht

Correspondence
michael.brecht@bccn-berlin.de (M.B.),
sh@hu-berlin.de (S.H.)

In brief
Gerhardt et al. develop the X-ray-visible neural tracer DiI-CT based on the well-established indocarbocyanine dye DiI. The authors demonstrate the dye's potential by examining the rat vibrissa follicle and uncover its neural 3D structure. Comparison of DiI-CT with its mother molecule shows unchanged fluorescent properties enabling bimodal neural imaging.

Highlights

- We added X-ray contrast to the neural tracer DiI via conjugation of iodine atoms

- The fluorescent properties of DiI-CT's mother molecule are preserved

- DiI-CT enables neural tracing in microCT scans to investigate neural 3D structure

- Samples can be sectioned post hoc for high-resolution fluorescence imaging

CellPress

Article

DiI-CT—A bimodal neural tracer for X-ray and fluorescence imaging

Ben Gerhardt,[1,4] Kristin Klaue,[2,4] Lennart Eigen,[1,4] Jutta Schwarz,[2,4] Stefan Hecht,[2,5,*] and Michael Brecht[1,3,5,6,*]

[1]Bernstein Center for Computational Neuroscience Berlin, Humboldt-Universität zu Berlin, Philippstr. 13, Haus 6, 10115 Berlin, Germany
[2]Department of Chemistry & IRIS/CSMB Adlershof, Humboldt-Universität zu Berlin, Brook-Taylor-Str.2, 12489 Berlin, Germany
[3]NeuroCure Cluster of Excellence, Humboldt-Universität zu Berlin, Unter den Linden 6, 10117 Berlin, Germany
[4]These authors contributed equally
[5]Senior author
[6]Lead contact
*Correspondence: michael.brecht@bccn-berlin.de (M.B.), sh@hu-berlin.de (S.H.)
https://doi.org/10.1016/j.crmeth.2023.100486

MOTIVATION Microfocus computed tomography (microCT) offers unique advantages for three-dimensional (3D) tissue analysis, but its contribution to neuroscience has been limited by the lack of neural tracers visible to X-rays. To address this problem, we developed a bimodal neural tracer for dual fluorescence and X-ray imaging.

SUMMARY

Here, we present an X-ray-visible neural tracer, referred to as DiI-CT, which is based on the well-established lipophilic indocarbocyanine dye DiI, to which we conjugated two iodine atoms. The tracer is visible with microfocus computed tomography (microCT) imaging and shares the excellent fluorescent tracing properties of DiI. We document the discovery potential of DiI-CT by analyzing the vibrissa follicle-sinus complex, a structure where visual access is poor and 3D tissue structure matters and reveal innervation patterns of the intact follicle in unprecedented detail. In the brain, DiI-CT tracing holds promise for verification evaluation of indirect connectivity measures, such as diffusion tensor imaging. We conclude that the bimodal dye DiI-CT opens new avenues for neuroanatomy.

INTRODUCTION

Ever since Golgi[1] and Cajal,[2] we know that visualization of neurons is fundamental for understanding brain function. In the last decades, we saw dramatic advances in the application of optical techniques to the brain. Indeed, an "age of light" in neurosciences has been proclaimed.[3] Such advances result from the synergistic effect of improved imaging techniques[4–6] in conjunction with advanced optical reporters (GFP,[7] synthetic and genetically encoded Calcium indicators[8,9]). Because the study of intact biological systems is of particular interest, tissue clearing efforts have boomed recently[10–13] to overcome challenges of deep tissue imaging posed by the strongly light-scattering brain tissue.

The current study focuses on the application of X-rays (i.e., microfocus computed tomography [microCT]) to neural circuits. Intrinsic properties of the short-wavelength and high-energy X-rays equip microCT with unique advantages of "seeing through" large bodies at high resolution while maintaining specimen integrity and have revolutionized morphological research.[14] X-ray-based assessment of bony structures in medical CT applications has long been used and is well established. Currently, we

are witnessing an explosive extension of X-ray-based techniques for the analysis of all kinds of biological (soft) tissues, resulting from advances in instrumentation and progress in interactive and (semi)automated image analysis and visualization.[15–18]

Despite such advances, the application of microCT to the brain is still in its infancy, and we argue that the lagging success of microCT is primarily due to a lack of neural tracers visible to X-rays. Hence, the development of an X-ray-visible neural tracer is the objective of our study. Our development did not start from scratch; instead we decided to build on an already established tracer. Specifically, we derived a tracer from the family of indocarbocyanine dyes, namely 1,1′-dihexadecyl-3,3,3′,3′-tetramethylindocarbo-cyanine perchlorate (DiI). DiI is a lipophilic tracer that attains extremely bright and stable fluorescence when embedded in lipid bilayers. Neural tracing with DiI had first been reported in the late 1980s, and it has since been proven to be an indispensable tool for visually aided decoding of cellular circuits in the brain and periphery.[19–23] The fluorescent properties of the DiI molecule originate from its π-conjugated cyanine system comprising two indoline rings, to which the name indocarbocyanine refers. Cell-specific DiI tracing results from the long alkyl chains (C16–C18), which are
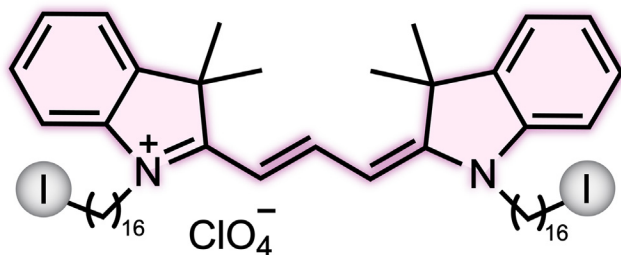
Figure 1. Molecular structure of DiI-CT
DiI-CT is a π-conjugated cyanine system (violet) comprising two indoline rings, each linked to a C_{16} alkyl chain via the respective nitrogen, that both contain a single iodine atom (gray) at the terminal carbon position.

the structural basis for the insertion of the molecule into the cell membrane, thus enabling lateral intramembrane diffusion analogous to a lipid raft.[24] Being well retained in the lipid bilayer, intermembrane diffusion of DiI (i.e., from one cell to another) rarely occurs. Excellent fluorescence, cell specificity, and the possibility to apply staining postmortem make DiI tracing extremely powerful.

Our strategy for attaining X-ray visibility was the integration of iodine atoms into DiI's molecular structure because iodine has a substantial X-ray cross-section, and we expected good X-ray visibility/contrast from such a modification. In modifying DiI, we aimed to retain the dye's excellent fluorescence properties to enable bimodal fluorescence and X-ray tracing. Therefore, we attached the iodine substituents to the terminals of DiI's long alkyl tails, far away from the dye core, to avoid quenching of its fluorescence because of the heavy atom effect (spin orbit coupling).

To assess the potential of our tracer, we repeated classical tracing applications in nerve and brain tissue and analyzed vibrissa follicle innervation. We chose to study the vibrissa follicle because our understanding of mechanotransduction of this sensory organ is greatly hampered by poor visual access to the intact follicle. There is, however, excellent neuroanatomical work of the sectioned follicle[25–27] that allowed us to evaluate our results.

In summary, we aimed to develop an X-ray-visible neural tracer and asked the following questions. (1) Can we impart DiI with X-ray visibility? (2) If so, does the DiI derivate retain its fluorescence? (3) How do fluorescence and X-ray imaging of the modified DiI compare? (4) Can the new dye help discover novel aspects of neural structure? We find that our novel X-ray-visible tracer, referred to as DiI-CT, meets the properties needed for microCT neural tracing.

RESULTS

Structure and synthesis of DiI-CT
DiI-CT was prepared in a two-step sequence involving initial *N*-alkylation of commercially available 2,3,3-trimethyl-*3H*-indol with 1,16-diiodohexadecane to obtain the monosubstituted 2,3,3-trimethyl-1-(16-iodohexadecyl)-*3H*-indolium iodide. Subsequent condensation of two equivalents of the indolium salt with one equivalent of triethyl orthoformate resulted in formation of the desired doubly iodinated trimethine carbocyanine dye DiI-CT (Figure 1). Structurally, DiI-CT resembles DiI, with the

important distinction of having two incorporated iodine atoms at the termini of the C16-alkyl chains.

Fluorescence properties of DiI-CT are practically identical to those of conventional DiI
The optical properties of DiI-CT were investigated in non-polar and polar solvents and compared with standard DiI under the same conditions (DiIC18(3), Sigma-Aldrich). The absorption and emission spectra of DiI-CT and DiI are identical in both solvents, with absorption maxima located at 563 nm (ε ≈ 147,000 L mol^{-1} cm^{-1}) and 551 nm (ε ≈ 136,000 L mol^{-1} cm^{-1}) and emission maxima located at 576 nm and 567 nm in benzene and ethanol, respectively (Figures 2A and 2B). Moreover, the fluorescence quantum yield and, thus, the excellent fluorescent tracing properties of DiI are retained upon introduction of iodine substituents at the alkyl chain termini (Figure 2C).

Staining properties of DiI-CT
To assess whether DiI-CT acts as a neuron-specific tracer, we compared its X-ray contrast properties with those of Lugol's solution (KI_3), which is a widely used protocol for soft tissue staining.[15] Specifically, we chose to study the tracing behavior in the pig infraorbital nerve (ION), a thick nerve containing highly myelinated axon bundles. The mass of iodine in 1 μL DiI-CT (30 mg/mL in 100% ethanol) solution was calculated, and KI_3 was diluted in 100% ethanol to contain either the same concentration of iodine (1× iodine) or 10 times as much (10× iodine) as the DiI-CT solution. Then, 1 μL of either solution was injected into a pig ION and scanned at serial time intervals (0 h, 2 h, and 24 h after injection) (Figure 3A). Comparison of the scans shows that the X-ray signal carried by DiI-CT specifically stays within the boundaries of the nerve bundles where it was injected (Figure 3B). Immediately after injection, the DiI-CT signal appears crisp and well defined, spreading along a distinct nerve bundle. After 2 h and 24 h of incubation, the dye further diffuses through the targeted nerve bundle without leaving it. The labeling stays bright, and a halo forms around it, indicating diffusion processes through the axon bundles. In contrast, microinjections of KI_3 solution appear rather diffuse from the start and spread over an area that is not restricted to the injection site (Figure 3C). Moreover, the injection of 1× iodine leaves only a weak signal at the injection site, which disappeared almost entirely between the 2 h and 24 h scanning interval (Figure 3C). The dramatic difference between the 2 h and the 24 h scan indicates a loss of X-ray signal as non-restricted diffusion processes through the whole tissue occur. The X-ray contrast of the 10× iodine injection is less intense than that of DiI-CT. While the signal is visible immediately after dye injection, the 2 h and 24 h time interval scans again show a rapid decrease in signal intensity (Figure 3D). The comparison of DiI-CT with 1× iodine and 10× iodine microinjections reveals markedly different staining properties of DiI-CT and KI_3 solution. We suggest that the staining behavior of DiI-CT reflects that of other lipophilic indocarbocyanine dyes, which enter and thus "stick" to membranes. Note that the type of repeated time-lapse imaging where samples are imaged at multiple instances cannot be done with conventional fluorescence DiI microscopy, where the sample needs to be sectioned for dye visualization.
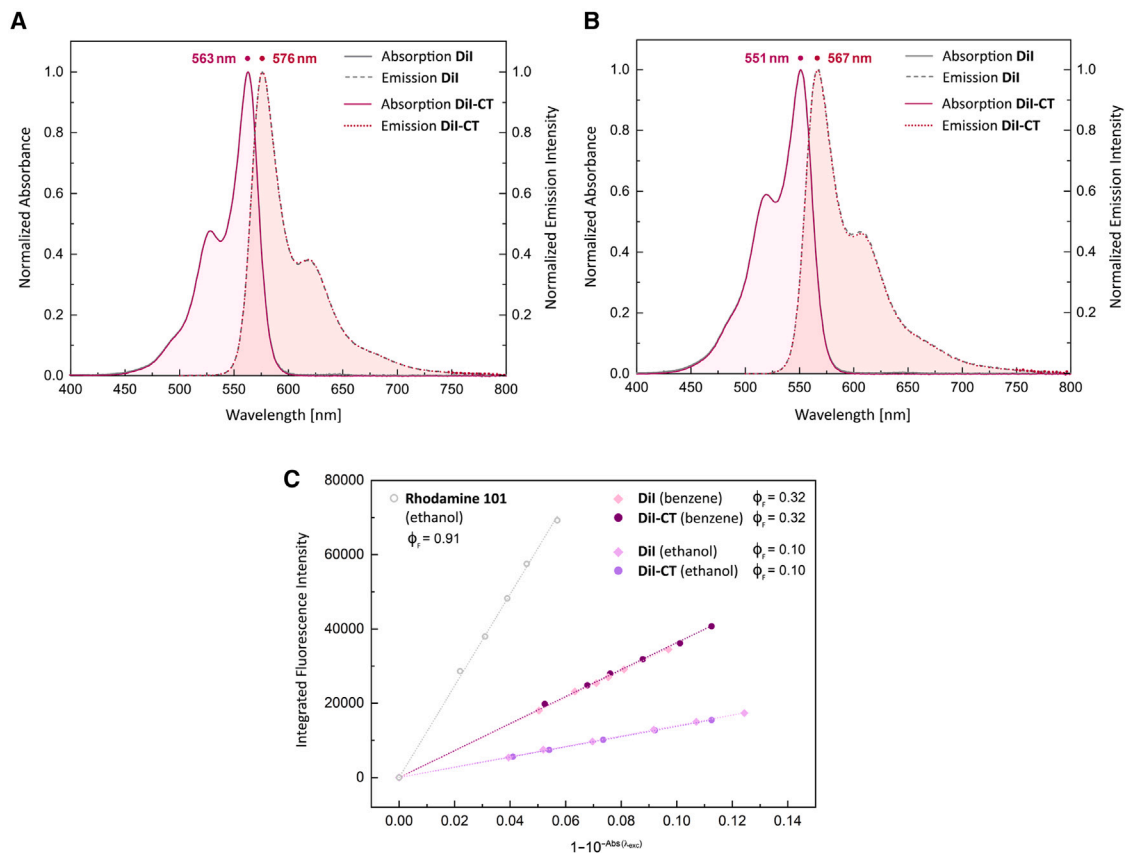
Figure 2. Fluorescence spectra and intensity of DiI-CT and DiI

(A and B) Normalized absorption and fluorescence spectra of DiI and DiI-CT in (A) benzene and (B) ethanol at 25°C. Absorbance and emission curves of DiI-CT and DiI (Figures S1 and S2), which match indistinguishably, are superimposed.

(C) Linear fits of corrected integrated fluorescence intensity versus $1 - 10^{Abs(\lambda_{exc})}$ for DiI-CT and DiI in benzene and ethanol, as well as Rhodamine 101 in ethanol as the fluorescence reference standard at 25°C and corresponding fluorescence quantum yields.

DiI-CT enables bimodal fluorescence and X-Ray imaging of nerve tissue

To better understand bimodal staining properties of DiI-CT, we compared its fluorescence with the X-ray contrast in the pig ION. 500 nL DiI-CT (45 mg/mL in 2:1 DMSO:ethanol) were injected into a 4 cm-long nerve at two spots, each 1 cm from the respective nerve ending. Subsequently, the sample was incubated at 45°C in 4% paraformaldehyde (PFA) and 0.1 M ethylenediaminetetraacetic acid (EDTA) in 0.1 M phosphate buffer (PB), and a microCT scan was performed 24 h after injection, followed by preparation of transverse and longitudinal cryosections of the same nerve sample for fluorescence microscopy. Alignment of transverse sections from fluorescence imaging (Figure 4A) and 2D virtual sections from microCT scans (Figure 4B) shows a DiI-CT signal within one nerve bundle. The DiI-CT fluorescence signal provides higher contrast than the microCT signal (Figure 4B) and readily allows identification of single fibers, which appear as ring-like staining patterns of myelin sheets (Figure 4A, inset). Under our experimental conditions (scans of centimeter-sized nerve tissue with an YXLON FF20 system), the DiI-CT signal was also highly localized in a subset of nerve bundles, but single-fiber resolution could not be achieved (Figure 4B, inset). We are confident, however, that

imaging of individual neurites can be achieved using long imaging times and high-end scanners or synchrotron sources. The DiI-CT fluorescence (Figure 4C) and X-ray imaging (Figure 4D) of longitudinal nerve sections lead to similar conclusions; both methods reveal highly localized and putatively identical staining patterns, where fluorescence imaging has a higher contrast and resolution. Bimodal imaging of the DiI-CT-stained ION reveals the different strengths of fluorescence and X-ray imaging. On one hand, there is extremely high contrast and resolution in the case of the fluorescence imaging of sections. Accordingly, fluorescence imaging outperforms X-ray imaging, where dye concentrations are low; i.e., at sites distal from the injection site. On the other hand, microCT imaging allows precise localization of staining in intact tissue.

DiI-CT based fluorescence neural tracing in brain tissue is equivalent to that of conventional DiI

To assess the fluorescence and staining behavior of DiI-CT, we compared its fluorescence characteristics with those of DiI in conventional neural tracing performed in brain tissue. To this end, we performed postmortem tracing in brains of stillborn piglets. More specifically, we injected equivalent amounts of DiI-CT
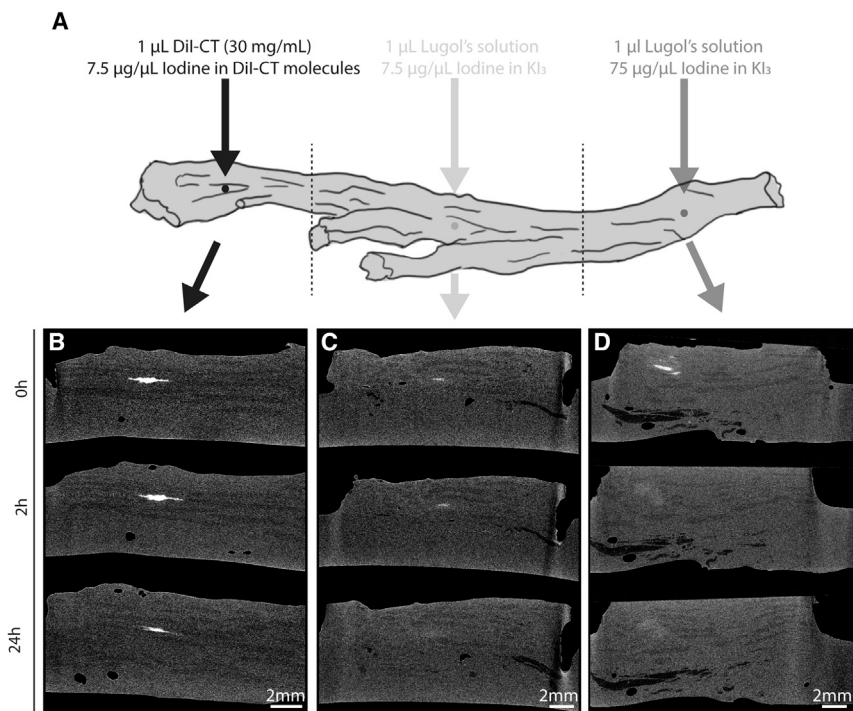
A

1 μL DiI-CT (30 mg/mL)
7.5 μg/μL Iodine in DiI-CT molecules

1 μl Lugol's solution
7.5 μg/μL Iodine in KI₃

1 μl Lugol's solution
75 μg/μL Iodine in KI₃

Figure 3. X-ray contrast and staining behavior of DiI-CT and iodine (KI₃) solution

(A) Schematic of DiI-CT and iodine (KI₃) injections into a pig ION.

(B–D) Time series of microCT scans of a pig ION (virtual longitudinal section) injected with (B) 1 μL DiI-CT containing 7.5 μg iodine in DiI-CT molecules, (C) 1 μL Lugol's solution containing 7.5 μg iodine, and (D) 1 μL Lugol's solution containing 75 μg iodine. Virtual sections were aligned by eye to each show the respective injection site, as illustrated in (A), 0 h, 2 h, and 24 h after dye injection. MicroCT scans were performed with the same parameters of 500-ms exposure time, 40 kV, and 110 μA and projections taken every 0.2° over continuous 360° rotation with a field of view corresponding to a cube with side lengths of 27.4 mm.

and DiI (500 nL, 45 mg/mL in 2:1 DMSO:ethanol, respectively) into the rostrum gyrus region, a brain region that receives dense thalamic input and has an enlarged cortical layer 4[28] (Figure 5A). We performed microCT as well as fluorescence imaging. As expected, only injection of DiI-CT leaves detectable contrast in microCT scans, while DiI cannot be seen with X-rays (Figure 5B). At the same time, both dyes show the same fluorescence staining properties; labeled cells express a strong fluorescence signal and allow visualization of neuronal migration through the brain tissue (Figure 5C). At the point where stained axons projecting from and to either gyrus merge, staining of both dyes is indiscriminate from one another (Figure 5D). High-resolution images of labeled neurons allow identification of individual cell morphology and sub-cellular features such as spines (Figures 5E and 5F). The findings corroborate our conclusions from Figure 2 and show that distal conjugation of iodine atoms indeed does not alter the molecule's fluorescence. We conclude that the fluorescence properties of DiI-CT are unchanged compared with DiI, but X-ray contrast is added.

In simultaneous staining experiments with DiI and DiI-CT, we did not observe an obvious difference in diffusion speed between the two dyes. One might expect slower diffusion of DiI-CT because of the conjugation of the two heavy iodine atoms, but our preliminary observations suggest that slow diffusion will not diminish the usefulness of DiI-CT.

DiI-CT based neural tracing reveals radially asymmetric innervation of the vibrissal follicle

The power and discovery potential of DiI-CT is most obvious when visual access is poor and 3D tissue structure is of significance. Such features apply to the follicle-sinus complex (FSC) in which

vibrissae are enrooted. The innervation pattern of the vibrissa follicle is thought to be of great functional significance. Specifically, it has been suggested that the arrangement of afferents around the vibrissa shaft might determine mechanotransduction and directional selectivity of afferents. We visualized the deep vibrissal nerve (DVN) in rats, a branch from the ION, which terminates inside the vibrissa follicle in mechanosensitive nerve endings to sense deflection of the vibrissae. To this end we injected 350 nL DiI-CT (45 mg/mL) into the DVN of an intact whisker pad and counter stained the whole sample in 1% PTA. Subsequently, we performed a microCT scan of the whole sample. A volume rendering reveals the grid-like arrangement of vibrissa follicles in the whisker pad (Figure 6A). DiI-CT injections in the DVN allowed visualization of the ascending nerve into the E3 follicle (Figure 6B). To better assess the quality of DiI-CT-based neural tracing, we extracted the E3 FSC for a high-resolution scan. The 3D volume rendering and planar views of the scanned FSC again show the same staining pattern as the whole whisker pad (Figures 6C and 6D). From these volume images we reconstructed the DiI-CT-stained DVN in high resolution and in the context of the other follicle elements (visualized roughly from the counterstaining; Figure 6E). Upon branching, the DVN forms 13 rather thick arms that are adjacent to the outer root sheath, which envelopes the hair shaft inside the inner root sheath and largely terminates at the beginning of the ring wulst, where it further subdivides into fine afferences (Figures 6E and 6F). The DVN arms do not engulf the vibrissa shaft evenly but rather form a radially asymmetric innervation pattern (Figure 6G). Surprisingly, the C-shaped formation of the nerve afferents remarkably matches mirror symmetrically with the C-shape of the ring wulst (Figure 6H). We conclude that DiI-CT reveals asymmetric follicle innervation and allows visualizing the innervation of the unsectioned follicle *in situ*.

DISCUSSION

We incorporated iodine atoms into the indocarbocyanine dye DiI and thus created a novel bimodal tracer, referred to as DiI-CT.
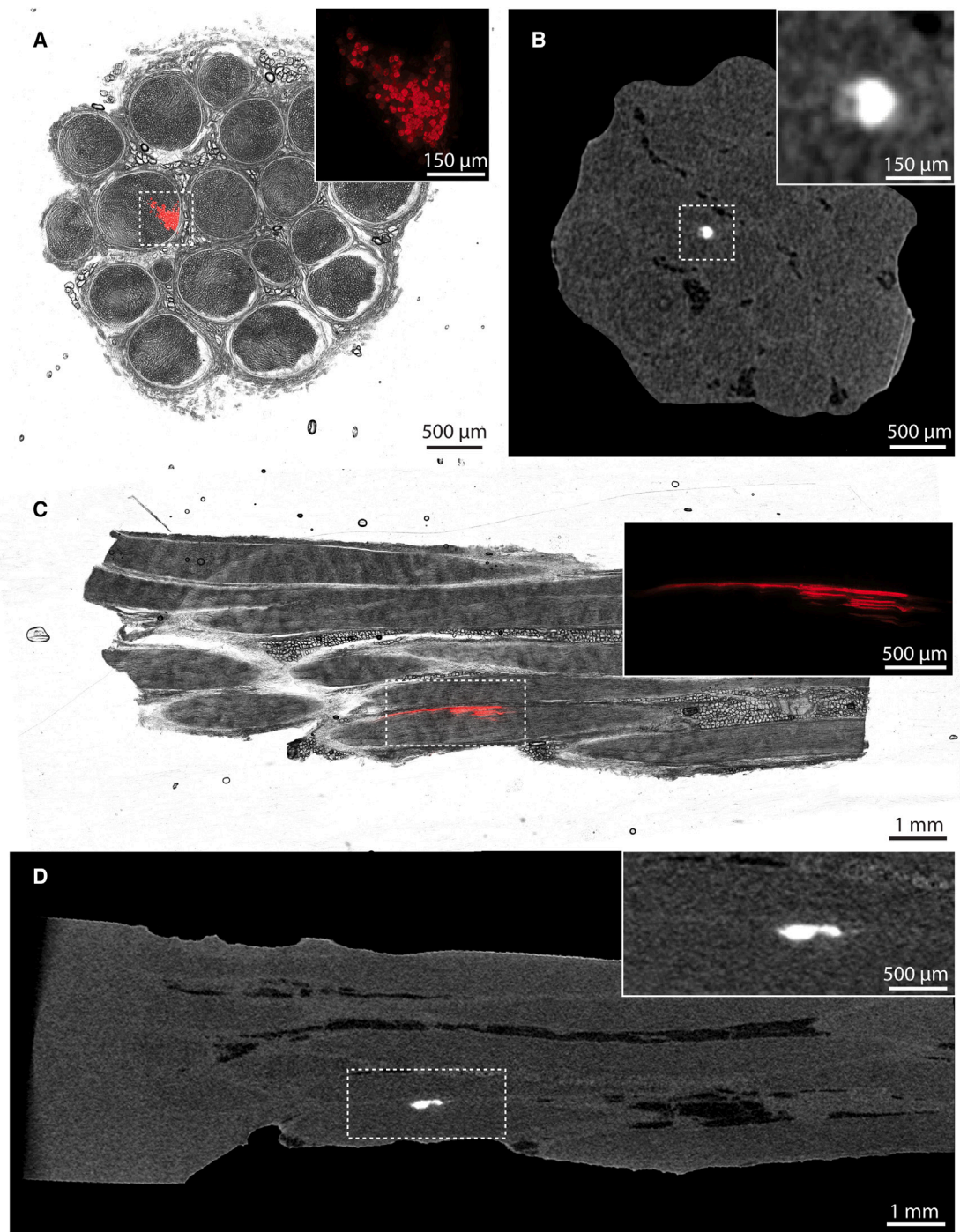
Figure 4. Bimodal fluorescence and X-ray imaging of nerve tissue with DiI-CT

(A and B) Alignment of a transverse section with (A) a bright-field image and red fluorescence superimposed and (B) microCT virtual transverse section of the same pig ION stained with DiI-CT. Insets show high magnification of the labeling, where accumulation of DiI-CT in myelin sheets can be observed with red fluorescence. DiI-CT X-ray signal spatially matches the fluorescent labeling, but single-fiber resolution was not achieved with the given scan.

(C and D) Alignment of a longitudinal section with (C) a bright-field image and red fluorescence superimposed and (D) microCT virtual longitudinal section of the same pig ION stained with DiI-CT.
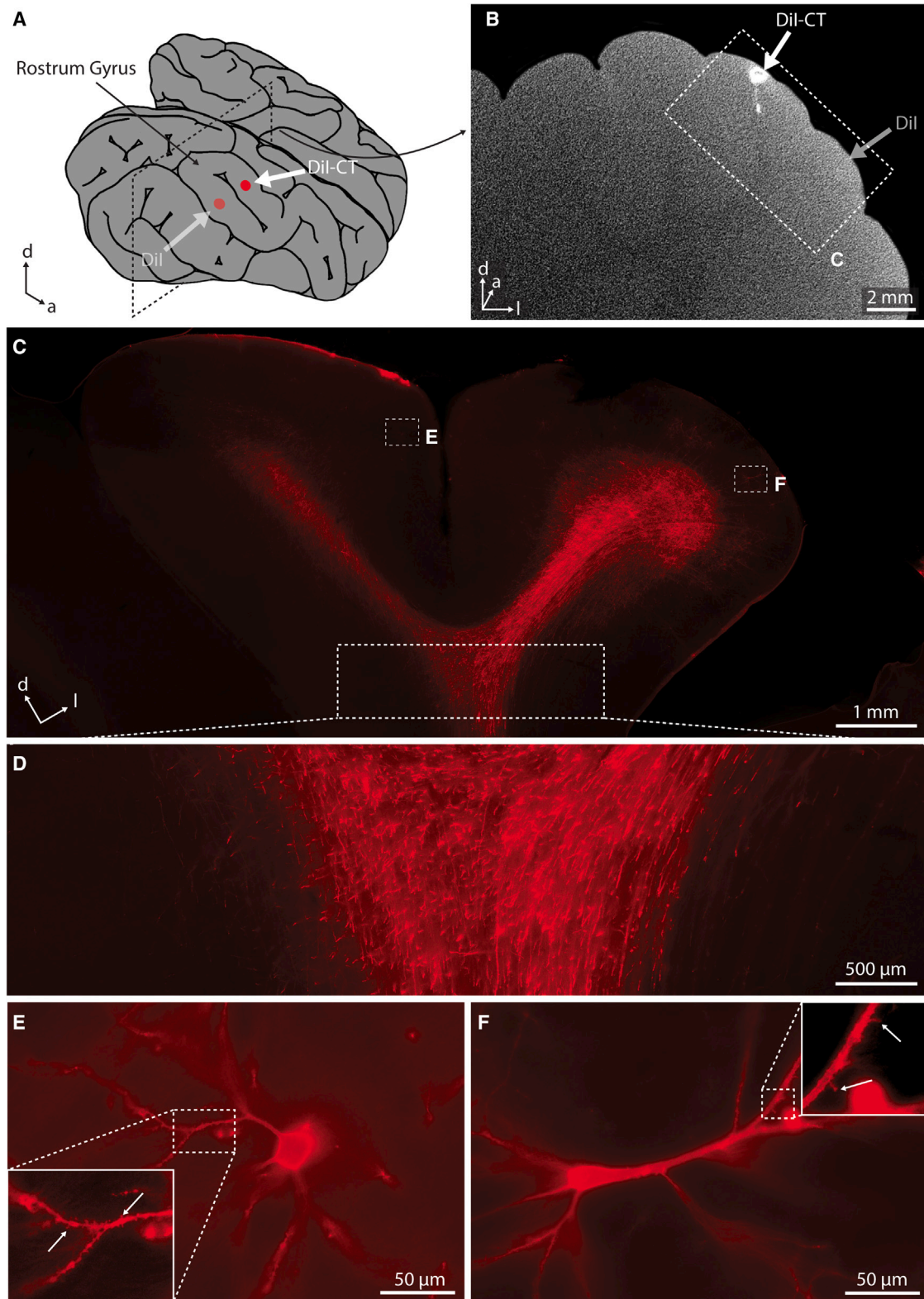
(legend on next page)

DiI-CT has excellent fluorescence and good X-ray visibility. The visual fluorescence brightness and contrast are superior to the brightness and contrast achieved in our microCT scans. We elucidate the 3D innervation pattern of the intact vibrissae follicle with DiI-CT, showcasing the discovery potential of our novel dye for neuroscience. We reckon that a design strategy similar to the one applied here (conjugation of iodine atoms) could also be used to convert other conventional neural dyes into X-ray-visible stains.

DiI-CT is a powerful bimodal dye

Our study shows unequivocally that DiI-CT is a powerful bimodal tracer. The fluorescence of DiI-CT is indistinguishable from that of DiI (Figures 2 and 5), arguably one of the most versatile fluorescent dyes used in neuroscience. In addition, the X-ray visibility of DiI-CT is introduced and spatially matches well with visual fluorescence (Figure 4). It is obvious that such bimodal properties will greatly facilitate the use of correlative fluorescence/X-ray approaches. Although correlative fluorescence/X-ray microscopy is also possible without a bimodal dye when very careful spatial alignment is performed, a bimodal dye clearly is the "silver bullet" for such work. It remains to be seen what results from such possibilities. It typically takes many years to fully establish a neural tracer. We expect, however, that this will not be the case for DiI-CT, as the application of this tracer builds upon decades of experience with DiI.

Limitations of the study

The biggest single limitation of DiI-CT is the limited brightness in microCT scans. Especially with conventional laboratory-based microCT systems, DiI-CT detection is still far from perfect. Nonetheless, we are optimistic about future perspectives for miniaturization of X-ray systems as recent developments have already successfully transitioned the coherence and brilliance of X-rays from synchroton facilities to laboratory setups.[29] Evidently, the brighter the dye, the easier detection will be. Other than that, DiI-CT shares the drawbacks of its parent DiI. Diffusion-driven tracing is slow, and maximum tracing distance is limited; cell specificity is good but not perfect, and the dye can bleach. These limitations are counterbalanced by the strength of DiI tracing: the ease of application, the brightness of the dye, and the ability to perform postmortem tracing. Further, it can be combined with histological techniques such as tissue clearing,[30] immunohistochemistry, and other conventional staining techniques. We reckon that postmortem tracing abilities will be particularly important because they reduce the need for animal experimentation.

DiI-CT elucidates the innervation of the vibrissa follicle

Our injections of DiI-CT solution into the DVN revealed the neuroarchitecture in remarkable detail. Specifically, we show that (E3) vibrissal innervation follows a strict 3D architecture. The DVN enters at fixed angles and does not grasp evenly but rather in a C-shaped motion around the whisker, mirroring the asymmetrical shape of the ring wulst[31] (Figure 6). The mechanical function of the ring wulst is thought to serve as a sensor for acceleration and deceleration of whisking motions in conjunction with its associated club-like nerve endings.[25,32] Dorsal to the C-shaped arm arrangement, beginning at the level of the ring wulst, the DiI-CT-stained fibers form a more homogeneous sheath of afferences around the whisker. The functional significance of the arm arrangement is unclear, but it is tempting to speculate that it sets radially distinct innervation territories that are instrumental in whisker deflection direction selectivity, one of the most prominent forms of response selectivity in trigeminal afferents.[33,34] As far as we can see, our holographic reconstructions of vibrissa innervation align well with reconstructions of the vibrissa follicle from serial sections,[31] and the match of microCT scans of DiI-CT stains and histological reconstruction gives confidence in our methodology. We conclude that DiI-CT holds enormous potential for the study of 3D innervation patterns.

Discovery potential of DiI-CT

It is difficult to assess the potential of a new method after using it for a short time only, and further work is required to realize the full potential of our novel dye. However, it is already obvious to us that DiI-CT will be particularly useful under specific circumstances. Where visual access is easy, resolution needs to be extremely high, and where 3D structure is not highly relevant, it will not be the dye of choice; hence we do not expect that DiI-CT will be used for spine imaging in slice preparations. Instead, where visual access is poor and where 3D structure matters, DiI-CT will prove advantageous, as we have shown for investigating the neuronal architecture of the vibrissa follicle. Other applications with intricate 3D structure and poor visual access are, for example, the cochlea, tooth innervation, or the insect antenna. We expect that DiI-CT can complement traditional methods for clarifying 3D structure[35] (Ragan et al.). We could also foresee that all kinds of deep tissue/long-time-lapse *in vivo* applications could be a promising field of study because microCT scans do not require sectioning. Thus, neuronal remodeling in metamorphosis could be one of the most interesting imaging application for DiI-CT. Another, perhaps more pressing field of application could be verification of indirect connectivity measures, such as diffusion tensor imaging;[36] many of these measures are being

---

Figure 5. Fluorescent neuronal labeling of DiI and DiI-CT is equivalent

(A) Piglet brain illustration with injection sites of DiI (lateral rostrum gyrus) and DiI-CT (medial rostrum gyrus).

(B) MicroCT scan coronal virtual section of a piglet brain injected with DiI (lateral rostrum gyrus) and DiI-CT (medial gyrus) and counterstained with 1% phosphotungstic acid (PTA). The field of view of the microCT scan corresponds to a cube with side lengths of 46 mm.

(C) Fluorescence image of the same piglet brain as in (B), zoomed in on the rostrum gyrus region as indicated with the inset in (B). Cells that are labeled with DiI or DiI-CT express strong fluorescence (red).

(D) DiI- and DiI-CT-stained axon bundles projecting from and to the rostrum gyrus region. Cells labeled with either dye cannot be told apart.

(E and F) (E) High magnification of a DiI-CT-stained pyramidal cell (left inset from C) and (F) a DiI-stained pyramidal cell (right inset from C). Fluorescent cell labeling through either dye allows identification of spines, a distinct sub-cellular feature (arrows in insets of E and F). d, dorsal; a, anterior; l, lateral.
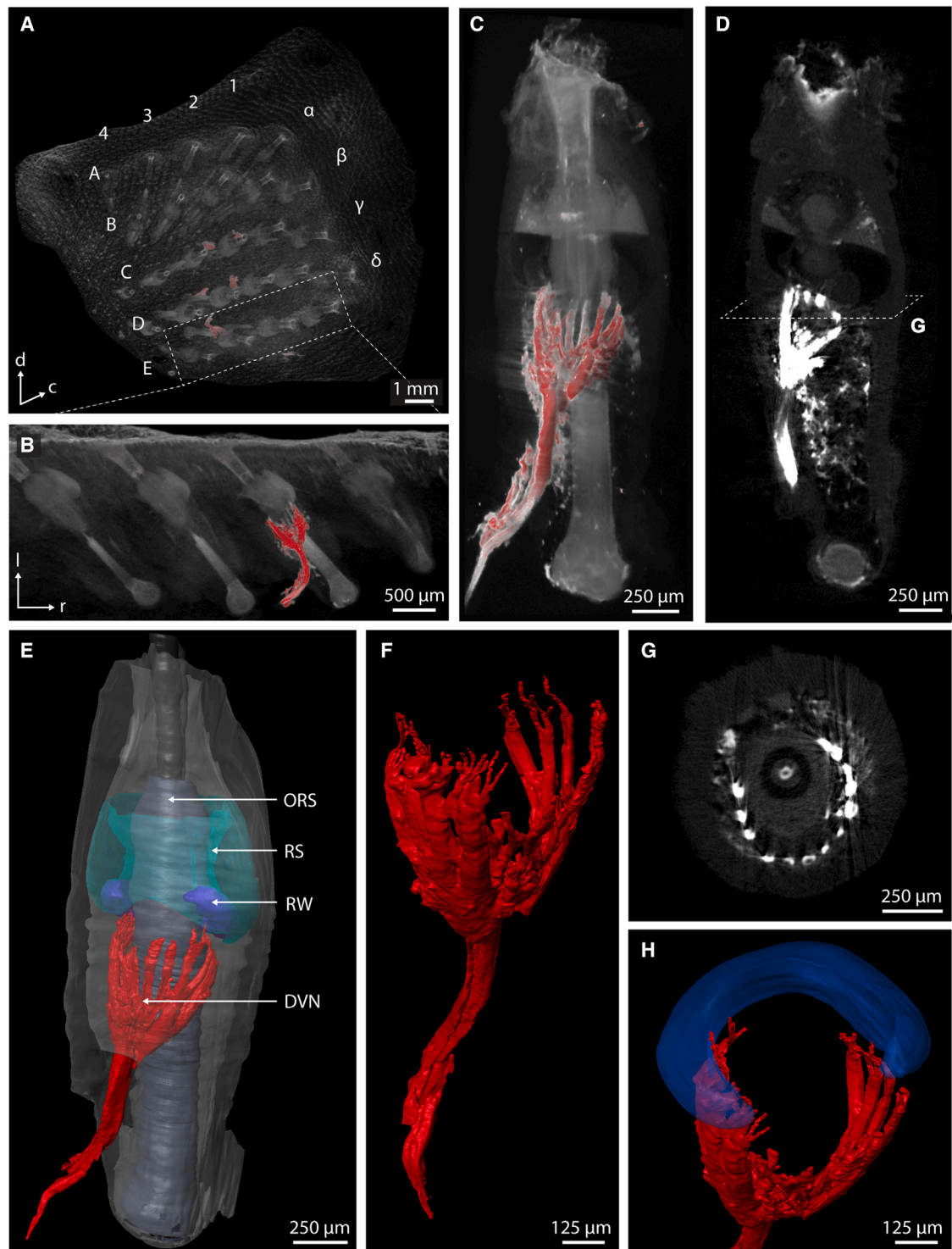
Figure 6. DiI-CT reveals radially asymmetric innervation of the vibrissa follicle

(A) MicroCT volume rendering of a rat left whisker pad. The grid-like architecture of the mystacial vibrissae was visualized by PTA counterstaining. Individual vibrissal nerves, labeled from DiI-CT microinjections, carry especially strong X-ray contrast and are shown in red.

(B) High magnification of the E row from the whisker pad in (A), showing the distinct innervation of the E3 follicle through DiI-CT labeling.

(C and D) 2D longitudinal virtual section (C) and 3D volume rendering (D) of the extracted E3 whisker follicle from (B).

(E) Segmentation of the E3 follicle, with key structures rendered in different colors (collagenous capsule in gray, outer root sheath [ORS] in purple, ring sinus [RS] in mint green, ring wulst [RW] in blue, deep vibrissal nerve [DVN] in red).

(legend continued on next page)

advanced without any ground-truth connectivity checks, and DiI-CT could help to resolve this problematic situation.

Conclusion

We describe a novel bimodal fluorescence/X-ray tracer. We are convinced that this and other improved staining methods, such as the coupling of gold nanoparticles to antibodies,[37] will pave the way for a stronger presence of microCT scanning in the neurosciences.

STAR★METHODS

Detailed methods are provided in the online version of this paper and include the following:

- KEY RESOURCES TABLE
- RESOURCE AVAILABILITY
  - Lead contact
  - Materials availability
  - Data and code availability
- EXPERIMENTAL MODEL AND SUBJECT DETAILS
- METHOD DETAILS
  - General methods and materials
  - DiI-CT synthesis and characterization
  - UV-vis and fluorescence spectroscopy
  - Carbocyanine tracing
  - Sample preparation for microCT scans
  - MicroCT imaging
  - Fluorescence imaging
  - Image post-processing
  - Animal sample origin and ethics
- QUANTIFICATION AND STATISTICAL ANALYSIS

AUTHOR CONTRIBUTIONS

Conceptualization, B.G., K.K., L.E., J.S., S.H., and M.B.; methodology & materials, B.G., K.K., L.E., J.S., S.H., and M.B.; investigation, B.G., K.K., L.E., J.S., S.H., and M.B.; formal analysis, B.G., K.K., and L.E.; writing, B.G., K.K., S.H., and M.B.; supervision, S.H. and M.B.; funding acquisition, S.H. and M.B.

REFERENCES

1. Golgi, C. (1873). Sulla struttura della sostanza grigia della cervello. Gazz. Med. Ital. Lobardia 6, 244–246.

2. Cajal, S.R.Y. (1888). Estructura de los centros nerviosos de las aves. Rev. Trum. Histol. Norm. Pat 1, 1–10.

3. Scanziani, M., and Häusser, M. (2009). Electrophysiology in the age of light. Nature 461, 930–939. https://doi.org/10.1038/nature08540.

4. Hell, S.W., and Wichmann, J. (1994). Breaking the diffraction resolution limit by stimulated emission: stimulated-emission-depletion fluorescence microscopy. Opt. Lett. 19, 780–782. https://doi.org/10.1364/ol.19.000780.

5. Denk, W., Strickler, J.H., and Webb, W.W. (1990). Two-photon laser scanning fluorescence microscopy. Science 248, 73–76. https://doi.org/10.1126/science.2321027.

6. Davidovits, P., and Egger, M.D. (1969). Scanning laser microscope. Nature 223, 831. https://doi.org/10.1038/223831a0.

7. Chalfie, M., Tu, Y., Euskirchen, G., Ward, W.W., and Prasher, D.C. (1994). Green fluorescent protein as a marker for gene expression. Science 263, 802–805. https://doi.org/10.1126/science.8303295.

8. Nakai, J., Ohkura, M., and Imoto, K. (2001). A high signal-to-noise Ca(2+) probe composed of a single green fluorescent protein. Nat. Biotechnol. 19, 137–141. https://doi.org/10.1038/84397.

9. Tian, L., Hires, S.A., Mao, T., Huber, D., Chiappe, M.E., Chalasani, S.H., Petreanu, L., Akerboom, J., McKinney, S.A., Schreiter, E.R., et al. (2009). Imaging neural activity in worms, flies and mice with improved GCaMP calcium indicators. Nat. Methods 6, 875–881. https://doi.org/10.1038/nmeth.1398.

10. Chung, K., Wallace, J., Kim, S.Y., Kalyanasundaram, S., Andalman, A.S., Davidson, T.J., Mirzabekov, J.J., Zalocusky, K.A., Mattis, J., Denisin, A.K., et al. (2013). Structural and molecular interrogation of intact biological systems. Nature 497, 332–337. https://doi.org/10.1038/nature12107.

11. Richardson, D.S., and Lichtman, J.W. (2015). Clarifying tissue clearing. Cell 162, 246–257. https://doi.org/10.1016/j.cell.2015.06.067.

12. Ertürk, A., Becker, K., Jährling, N., Mauch, C.P., Hojer, C.D., Egen, J.G., Hellal, F., Bradke, F., Sheng, M., and Dodt, H.U. (2012). Three-dimensional imaging of solvent-cleared organs using 3DISCO. Nat. Protoc. 7, 1983–1995. https://doi.org/10.1038/nprot.2012.119.

13. Dodt, H.U., Leischner, U., Schierloh, A., Jährling, N., Mauch, C.P., Deininger, K., Deussing, J.M., Eder, M., Zieglgänsberger, W., and Becker, K. (2007). Ultramicroscopy: three-dimensional visualization of neuronal networks in the whole mouse brain. Nat. Methods 4, 331–336. https://doi.org/10.1038/nmeth1036.

(F) Magnified reconstruction of the DVN innervating the E3 follicle, revealing the branching behavior into 13 thick arms, which further subdivide into ∼30 fine afferences.

(G) 2D transverse virtual section of the E3 FSC inferior to the ring wulst, as shown in (D), shows radially asymmetric distribution of the afferent innervation around the vibrissa shaft circumference.

(H) Oblique view of the radially asymmetric branches of the DVN branches and the ring wulst. This remarkably asymmetric innervation pattern with two opposing C shapes of the RW and nerve branches was seen in all DiI-CT-injected follicles. ORS, outer root sheath; c, caudal; l, lateral; r, rostral.

14. Cunningham, J.A., Rahman, I.A., Lautenschlager, S., Rayfield, E.J., and Donoghue, P.C.J. (2014). A virtual world of paleontology. Trends Ecol. Evol. *29*, 347–357. https://doi.org/10.1016/j.tree.2014.04.004.

15. Metscher, B.D. (2009). MicroCT for comparative morphology: simple staining methods allow high-contrast 3D imaging of diverse non-mineralized animal tissues. BMC Physiol. *9*, 11. https://doi.org/10.1186/1472-6793-9-11.

16. Bartels, M., Krenkel, M., Cloetens, P., Möbius, W., and Salditt, T. (2015). Myelinated mouse nerves studied by X-ray phase contrast zoom tomography. J. Struct. Biol. *192*, 561–568. https://doi.org/10.1016/j.jsb.2015.11.001.

17. Töpperwien, M., Krenkel, M., Vincenz, D., Stöber, F., Oelschlegel, A.M., Goldschmidt, J., and Salditt, T. (2017). Three-dimensional mouse brain cytoarchitecture revealed by laboratory-based x-ray phase-contrast tomography. Sci. Rep. *7*, 42847. https://doi.org/10.1038/srep42847.

18. Walsh, C.L., Tafforeau, P., Wagner, W.L., Jafree, D.J., Bellier, A., Werlein, C., Kühnel, M.P., Boller, E., Walker-Samuel, S., Robertus, J.L., et al. (2021). Imaging intact human organs with local resolution of cellular structures using hierarchical phase-contrast tomography. Nat. Methods *18*, 1532–1541. https://doi.org/10.1038/s41592-021-01317-x.

19. Honig, M.G., and Hume, R.I. (1986). Fluorescent carbocyanine dyes allow living neurons of identified origin to be studied in long-term cultures. J. Cell Biol. *103*, 171–187. https://doi.org/10.1083/jcb.103.1.171.

20. Burkhalter, A., and Bernardo, K.L. (1989). Organization of corticocortical connections in human visual cortex. Proc. Natl. Acad. Sci. USA *86*, 1071–1075. https://doi.org/10.1073/pnas.86.3.1071.

21. Li, Y., Song, Y., Zhao, L., Gaidosh, G., Laties, A.M., and Wen, R. (2008). Direct labeling and visualization of blood vessels with lipophilic carbocyanine dye DiI. Nat. Protoc. *3*, 1703–1708. https://doi.org/10.1038/nprot.2008.172.

22. Vidal-Sanz, M., Villegas-Pérez, M.P., Bray, G.M., and Aguayo, A.J. (1988). Persistent retrograde labeling of adult rat retinal ganglion cells with the carbocyanine dye diI. Exp. Neurol. *102*, 92–101. https://doi.org/10.1016/0014-4886(88)90081-7.

23. Mufson, E.J., Brady, D.R., and Kordower, J.H. (1990). Tracing neuronal connections in postmortem human hippocampal complex with the carbocyanine dye DiI. Neurobiol. Aging *11*, 649–653. https://doi.org/10.1016/0197-4580(90)90031-t.

24. Lai, H.M., Ng, W.L., Gentleman, S.M., and Wu, W. (2017). Chemical probes for visualizing intact animal and human brain tissue. Cell Chem. Biol. *24*, 659–672. https://doi.org/10.1016/j.chembiol.2017.05.015.

25. Ebara, S., Kumamoto, K., Matsuura, T., Mazurkiewicz, J.E., and Rice, F.L. (2002). Similarities and differences in the innervation of mystacial vibrissal follicle-sinus complexes in the rat and cat: a confocal microscopic study. J. Comp. Neurol. *449*, 103–119. https://doi.org/10.1002/cne.10277.

26. Rice, F.L., Mance, A., and Munger, B.L. (1986). A comparative light microscopic analysis of the sensory innervation of the mystacial pad. I. Innervation of vibrissal follicle-sinus complexes. J. Comp. Neurol. *252*, 154–174. https://doi.org/10.1002/cne.902520203.

27. Maklad, A., Fritzsch, B., and Hansen, L.A. (2004). Innervation of the maxillary vibrissae in mice as revealed by anterograde and retrograde tract tracing. Cell Tissue Res. *315*, 167–180. https://doi.org/10.1007/s00441-003-0816-z.

28. Ritter, C., Maier, E., Schneeweiß, U., Wölk, T., Simonnet, J., Malkawi, S., Eigen, L., Tunckol, E., Purkart, L., and Brecht, M. (2021). An isomorphic three-dimensional cortical model of the pig rostrum. J. Comp. Neurol. *529*, 2070–2090. https://doi.org/10.1002/cne.25073.

29. Eckermann, M., Töpperwien, M., Robisch, A.L., van der Meer, F., Stadelmann, C., and Salditt, T. (2020). Phase-contrast x-ray tomography of neuronal tissue at laboratory sources with submicron resolution. J. Med. Imaging *7*, 013502. https://doi.org/10.1117/1.JMI.7.1.013502.

30. Hou, B., Zhang, D., Zhao, S., Wei, M., Yang, Z., Wang, S., Wang, J., Zhang, X., Liu, B., Fan, L., et al. (2015). Scalable and DiI-compatible optical clearance of the mammalian brain. Front. Neuroanat. *9*, 19. https://doi.org/10.3389/fnana.2015.00019.

31. Kim, J.N., Koh, K.S., Lee, E., Park, S.C., and Song, W.C. (2011). The morphology of the rat vibrissal follicle-sinus complex revealed by three-dimensional computer-aided reconstruction. Cells Tissues Organs *193*, 207–214. https://doi.org/10.1159/000319394.

32. Whiteley, S.J., Knutsen, P.M., Matthews, D.W., and Kleinfeld, D. (2015). Deflection of a vibrissa leads to a gradient of strain across mechanoreceptors in a mystacial follicle. J. Neurophysiol. *114*, 138–145. https://doi.org/10.1152/jn.00179.2015.

33. Lichtenstein, S.H., Carvell, G.E., and Simons, D.J. (1990). Responses of rat trigeminal ganglion neurons to movements of vibrissae in different directions. Somatosens. Mot. Res. *7*, 47–65. https://doi.org/10.3109/08990229009144697.

34. Hattox, A.M., Priest, C.A., and Keller, A. (2002). Functional circuitry involved in the regulation of whisker movements. J. Comp. Neurol. *442*, 266–276. https://doi.org/10.1002/cne.10089.

35. Ragan, T., Kadiri, L.R., Venkataraju, K.U., Bahlmann, K., Sutin, J., Taranda, J., Arganda-Carreras, I., Kim, Y., Seung, H.S., and Osten, P. (2012). Serial two-photon tomography for automated ex vivo mouse brain imaging. Nat. Methods *9*, 255–258. https://doi.org/10.1038/nmeth.1854.

36. Le Bihan, D., Mangin, J.F., Poupon, C., Clark, C.A., Pappata, S., Molko, N., and Chabriat, H. (2001). Diffusion tensor imaging: concepts and applications. J. Magn. Reson. Imag. *13*, 534–546. https://doi.org/10.1002/jmri.1076.

37. Depannemaecker, D., Santos, L.E.C., de Almeida, A.C.G., Ferreira, G.B.S., Baraldi, G.L., Miqueles, E.X., de Carvalho, M., Costa, G.S.R., Marques, M.J.G., Scorza, C.A., and Rinkel, J. (2019). Gold nanoparticles for X-ray microtomography of neurons. ACS Chem. Neurosci. *10*, 3404–3408. https://doi.org/10.1021/acschemneuro.9b00290.

38. Wang, H., Huang, J., Wulff, W.D., and Rheingold, A.L. (2003). The first examples of a meta-benzannulation from the reaction of Fischer carbene complexes with alkynes. J. Am. Chem. Soc. *125*, 8980–8981. https://doi.org/10.1021/ja035428n.

39. Würth, C., Grabolle, M., Pauli, J., Spieles, M., and Resch-Genger, U. (2013). Relative and absolute determination of fluorescence quantum yields of transparent samples. Nat. Protoc. *8*, 1535–1550. https://doi.org/10.1038/nprot.2013.087.

40. Melnychuk, N., Egloff, S., Runser, A., Reisch, A., and Klymchenko, A.S. (2020). Light-harvesting nanoparticle probes for FRET-based detection of oligonucleotides with single-molecule sensitivity. Angew. Chem., Int. Ed. *59*, 6811–6818.

41. Sparks, D.L., Lue, L.F., Martin, T.A., and Rogers, J. (2000). Neural tract tracing using Di-I: a review and a new method to make fast Di-I faster in human brain. J. Neurosci. Methods *103*, 3–10. https://doi.org/10.1016/s0165-0270(00)00291-0.

42. Lukas, J.R., Aigner, M., Denk, M., Heinzl, H., Burian, M., and Mayr, R. (1998). Carbocyanine postmortem neuronal tracing. Influence of different parameters on tracing distance and combination with immunocytochemistry. J. Histochem. Cytochem. *46*, 901–910. https://doi.org/10.1177/002215549804600805.

43. Hofmann, M.H., and Bleckmann, H. (1999). Effect of temperature and calcium on transneuronal diffusion of DiI in fixed brain preparations. J. Neurosci. Methods *88*, 27–31. https://doi.org/10.1016/s0165-0270(99)00007-2.

Cell Reports Methods
Article

STAR★METHODS

KEY RESOURCES TABLE

REAGENT or RESOURCE	SOURCE	IDENTIFIER
Biological samples		
Stilborn Piglets	Agrargenossenschaft Groß Machnow	N/A
Pig heads	Willi Hofner Fleischgroßhandel	N/A
Long Evan Rats	Janvier	Strain Code: 006
Chemicals, peptides, and recombinant proteins		
DiIC18(3)	Sigma Aldrich	Cat. # 41085-99-8
DiI-CT	This paper	N/A
Formaldehyde	Carl Roth	Cat. # 0335.3
Dimethylsulfoxid	Carl Roth	Cat. # A994.1
Ethylenediaminetetraacetic acid	Carl Roth	Cat. # 8040.1
Phosphotungstic acid hydrate	Sigma Aldrich	Cat. # 79690-100G
Ethanol	Carl Roth	Cat. # 5054.3
Phosphorus pentoxide	Sigma Aldrich	Cat. # 79610-500g
Orthophosphoric acid	FisherSci	Cat. # 15823030
Argon	Sigma Aldrich	Cat. # 7440-37-1
Potassium iodide	Sigma Aldrich	Cat. # 221945-500G
1,16-hexadecandiol	TCI	Cat. #H0552
Thiosulfate	Roth	Cat. # HN25.3
Magnesium sulfate	Grüssing	Cat. # 120941000
Acetonitrile	VWR	Cat. # 83640.320
2,3,3-trimethylindolenine	TCI	Cat. #T0766
Triethyl orthoformate	Sigma Aldrich	Cat. # 304050-1L
Acetic anhydride	Grüssing	Cat. # 102981000
Formic acid	FisherSci	Cat. # 15603870
Perchloric acid	FisherSci	Cat. # 15214924
Benzene	TCI	Cat. #B0020
Rhodamine 101	Sigma Aldrich	Cat. # 83694-500mg
Iodine-Potassium-Iodide (Lugol's Solution)	Morphisto	Cat. # 10255
Critical commercial assays		
Silica Gel 60 for Column chromatography	VWR	Cat. # 717177-25kg
Silica Gel 254 for thin-layer chromatography	Supelco/Merck	Cat. # 105554
Software and algorithms		
Amira ZIBE Edition 2022.17	Thermo Scientific	https://thermofisher.com/amira-avizo
Dragonfly ORS 2021.3	Object Research Systems	https://www.theobjects.com/dragonfly
Other		
YXLON FF20 CT system	YXLON International	https://yxlon.comet.tech/de/products-de/ff20-ct

RESOURCE AVAILABILITY

Lead contact
Further information and requests for resources and reagents should be directed to and will be fulfilled by the lead contact Michael Brecht (michael.brecht@bccn-berlin.de).

Materials availability
In this study a new dye – DiI-CT – was developed as described in the methods section. We intend to make it available for the broad scientific community. Requests should be directed to the lead contact.

Data and code availability

- The data that supports the findings of the study, i.e., microCT scans, fluorescence images, and spectroscopy data and fluorescence measurements are available upon request. Figures are openly available in G-Node GIN at https://gin.g-node.org/elephant/DiICT.
- The paper does not report any original code.
- Any additional information required to reanalyze the data reported in this paper is available from the lead contact upon request.

EXPERIMENTAL MODEL AND SUBJECT DETAILS

Cadaver of 5–6 week old, male Long Evan rats were used for preparations of follicle injections. Cadaver of adult domesticated pigs of unknown exact age and unknown sex were used for infraorbital nerve preparations. Still born 1-day postnatal piglets of unknown sex were used for brain preparations.

METHOD DETAILS

General methods and materials

Starting materials and reagents were used as received from Sigma-Aldrich, TCI, ABCR, or Fischer Scientific without further purification unless noted otherwise. Ethyl acetate (EA), diethyl ether, and petroleum ether (PE) were distilled before usage. Thin-layer chromatography (TLC) was performed on commercial Merck 60F, 254 silica gel plates, and compounds were visualized with the naked eye or UV light (λ = 254 nm). Column chromatography was carried out with silica gel (Merck 60, particle size 0.040–0.063 mm) using eluents as specified. Preparative HPLC was conducted using a Waters 996 Photodiode Array Detector and Waters Fraction Collector III connected to a Waters 600 Controller on a phenylhexyl (PhHex) reverse phase column (Luna 5 μm LC column 250 × 20 mm) with acetonitrile/water mixtures (20 mL/min flow), degassed by a constant helium purge and a Knauer degasser. NMR spectra were recorded on a Bruker DPX 500 Spectrometer (500 MHz for ^{1}H, 126 MHz for ^{13}C) at 25°C using residual protonated solvent signals as internal standard (^{1}H: δ(CDCl$_3$) = 7.26 ppm; δ(CD$_3$CN) = 1.94 ppm; 13C: δ(C$_6$D$_6$) = 128.1 ppm, δ(CDCl$_3$) = 77.2 ppm; δ(CD$_3$CN) = 118.3 ppm, 1.3 ppm). Coupling constants J, are denoted in Hz. The splitting patterns are abbreviated as follows: singlet (s), doublet (d), triplet (t), quadruplet (q), multiplet (m), doublet of doublets (dd), triplet of doublets (td), and broad (br). Ultra-Performance Liquid Chromatography (UPLC) measurements were performed on a Waters UPLC Acquity equipped with an Acquity QDa Detector for UPLC-MS in combination with a PDA eλ detector, using reversed phase (Acquity UPLC BEH C18 1.7 μm (2.1 × 50 mm) or Acquity UPLC BEH Phenyl 1.7 μm (2.1 × 100 mm)) columns operated at 35°C with solvent gradients of 80%–5% water with 0.1% formic acid and 20%–95% acetonitrile with 0.1% formic acid.

DiI-CT synthesis and characterization

1,16-Diiodohexadecane

Phosphorus pentoxide (2.73 g, 19.3 mmol) was dissolved in 9.2 mL of phosphoric acid (85 wt % in H$_2$O) and purged with argon. Afterward, potassium iodide (13.26 g, 80.0 mmol) was added in portions under vigorous stirring, followed by the addition of 1,16-hexa-decandiol (3.56 g, 13.8 mmol). The resulting reaction mixture was heated to 115°C for 2.5 h. After cooling to room temperature, water and diethyl ether were added to the solution and the organic phase was separated, washed with 10% aq. thiosulfate solution, dried over anhydrous magnesium sulfate and evaporated under reduced pressure. Column chromatography (silica, PE) afforded the desired product as a pale orange solid (5.95 g, 12.4 mmol, 90%). The analytical data is in accordance with the literature.[38]

2,3,3-Trimethyl-1-(16-iodohexadecyl)-3H-indolium iodide

2,3,3-Trimethylindo-lenine was purified by column chromatography (silica gel, PE/EA 1:1) directly before use. 1,16-Diiodohexadecane (5.94 g, 12.4 mmol) was dissolved in acetonitrile upon heating, 2,3,3-trimethylindolenine (1.65 g, 10.4 mmol) was added and heated to reflux for 2 days. After cooling to room temperature, the reaction mixture was washed several times with petroleum ether, dried over anhydrous magnesium sulfate, and evaporated under reduced pressure. The residue was suspended and stirred in diethyl ether for 30 min. The resulting precipitate was filtered off and the disubstituted byproduct was removed by recrystallization from ethyl acetate to obtain the desired product as a mauve solid (1.25 g, 10.4 mmol, 20%).

^{1}H-NMR (500 MHz, CD$_3$CN): δ = 7.81–7.74 (m, 1H), 7.76–7.69 (m, 1H), 7.67–7.58 (m, 2H), 4.40–4.34 (m, 2H), 3.24 (t, J = 7.0 Hz, 2H), 2.75 (s, 3H), 1.93–1.85 (m, 2H), 1.78 (p, J = 7.1 Hz, 2H), 1.55 (s, 6H), 1.50–1.40 (m, 2H), 1.41–1.31 (m, 4H), 1.32–1.22 (m, 18H) ppm.

^{13}C-NMR (126 MHz, CD$_3$CN): δ = 197.1, 143.0, 142.1, 130.9, 130.2, 124.5, 116.4, 55.6, 49.4, 34.3, 31.1, 30.3, 30.3, 30.2, 30.1, 30.1, 30.0, 29.7, 29.1, 28.4, 27.2, 22.7, 15.1, 8.6 ppm.

DiI-CT

2,3,3-Trimethyl-1-(16-iodohexadecyl)-3H-indoliumiodid (191 mg, 0.30 mmol) and freshly distilled triethyl orthoformate (0.25 mL, 0.15 mmol) were dissolved in 2.0 mL of acetic anhydride and heated to reflux for 8 h until the UPLC showed complete consumption of the starting material. Afterward, the solvent was removed, and the crude product was purified by preparative HPLC (PhHex, acetonitrile with 1% v/v formic acid/Milli-Q water 90:10 to 95:5). After evaporation of the solvent mixture, the product was redissolved in a

small amount of acetonitrile and a slight excess of perchloric acid was added dropwise. Finally, ethyl acetate was added, and the organic phase was washed with water until the remaining acid was removed. The organic phase was dried over anhydrous magnesium sulfate and evaporated under reduced pressure to yield DiI-CT (80 mg, 0.07 mmol, 47%) as a crystalline pink solid. ^{1}H-NMR (500 MHz, CD_3CN): $\delta = 8.44$ (t, $J = 13.5$ Hz, 1H), 7.52 (dd, $J = 7.3, 1.3$ Hz, 2H), 7.43 (td, $J = 7.7, 1.2$ Hz, 2H), 7.30 (t, $J = 7.8$ Hz, 4H), 6.32 (d, $J = 13.5$ Hz, 2H), 4.03 (t, $J = 7.6$ Hz, 4H), 3.23 (t, J = 7.0 Hz, 4H), 1.83–1.73 (m, 8H), 1.71 (s, 12H), 1.47–1.40 (m, 4H), 1.40–1.32 (m, 8H), 1.30–1.22 (m, 36H) ppm (Figure S3).

^{13}C-NMR (126 MHz, C_6D_6): $\delta = 173.8, 151.0, 142.7, 141.0, 129.0, 125.1, 122.1, 111.5, 105.5, 48.9, 44.9, 33.9, 30.8, 30.3, 30.2, 30.2, 30.1, 30.1, 30.0, 29.9, 28.9, 28.3, 27.9, 27.1, 7.1$ ppm (Figure S4). MS(ESI+): m/z calculated for $C_{55}H_{87}I_2N_2{}^+$ 1029.495, found 1029.496 (Figure S5).

UV-vis and fluorescence spectroscopy

UV-vis spectroscopy was performed on an Agilent Cary 50 instrument connected to a cryostat from Quantum Northwest, Modell Luma 40 (temperature accuracy ±0.15 K) in 10 × 10 mm quartz cuvettes with 3 mL volume. Fluorescence spectra were recorded on a Varian Cary Eclipse Fluorescence Spectrometer and corrected for variations in wavelength dependent photomultiplier response using correction curves generated on the instrument. For all spectroscopy experiments, non-degassed solvents of spectroscopy grade were used.

Fluorescence quantum yields (φ_F) were determined according to:

$$\varphi_F(X) = \varphi_F(Ref) \cdot \frac{m_X}{m_{Ref}} \cdot \frac{\eta_X{}^2}{\eta_{Ref}{}^2}$$

the subscripts X and Ref denote unknown samples and references, m depicts the slope from the linear fit of integrated fluorescence intensity versus $1 - 10^{Abs(\lambda_{exc})}$ at the excitation wavelength (which was kept constant for the sample and reference), and η is the refractive index of the used solvents. Rhodamine 101 in ethanol was used as reference ($\varphi_F = 0.91$).[39]

The fluorescence quantum yields for DiI-CT and DiI are 0.32 in benzene and 0.10 in ethanol at 25°C. The value for DiI in ethanol is in accordance with the literature.[40]

Carbocyanine tracing

DiI-CT or DiI (DiIC18(3), Sigma Aldrich) was diluted in either 100% ethanol or a 2:1 mixture of dimethyl sulfoxide (DMSO) and ethanol containing 30–45 mg/mL. The solution was sonicated in a water bath at 50°C for 15 min and vortexed extensively.

Microinjections of the dye solution were performed using glass pipettes attached to a stereotaxic micro-manipulator (Narishige International, London UK). 10 μL Pipettes (Drummond Scientific, Broomall USA) were pulled to a tip diameter of 1 μm with a Sutter Instrument P-97 pipette puller and punched through a Kimtech tissue, resulting in 8-13 μm sharp-edged pipette tips with a 1 mm taper. Smaller tips do not allow loading of the viscous dye solution and bigger tips result in imprecise dye delivery.

The dye was injected into either 4% paraformaldehyde (PFA) fixed (all peripheral structures) or fresh tissue (brains) and fixed in 4% PFA with a delay to improve the rate of dye diffusion.[41] The tissue was stabilised by embedding in 4% agarose or fixed in position using needles. Subsequently, volumes of 250–1000 nL dye were injected manually using a hydraulic injector (Narishige International, London UK) at rates of 1–5 min/100 nL. To avoid leakage of the dye, injection spots were sealed by application of 4% agarose to the injection site. Injected samples were incubated at 45°C to accelerate dye diffusion[42] in 4% PFA and 0.1 M ethylenediaminetetraacetic acid (EDTA) in 0.1 M phosphate buffer (PB). Additive of EDTA to the fixation medium improves the staining quality of DiI.[43]

Sample preparation for microCT scans

Brains were placed in a small plastic container and then fully covered in 4% agarose. Whole whisker pad and infraorbital nerve samples were embedded in a layer of 4% agarose in a Petri dish, cut out in a wedge shape, and stuck into a 25 mL falcon tube. Single follicle and whisker pad rows were placed in 10–200 μL pipette tips, filled with 1% agarose, and sealed with Parafilm to prevent evaporation during the scanning process. Sample holders containing the samples were then mounted onto the scanner's manipulator directly or using a Goniometer for high precision scans of small samples.

To allow visualization of all structures within the specimen, samples were counter-stained in 1% phosphotungstic acid (PTA) for 24 h to 1 week.[15] PTA proved to not interfere with the dye's fluorescence, which is crucial for upholding the bimodality of DiI-CT.

MicroCT imaging

MicroCT scans were performed with a YXLON FF20 CT system (YXLON International GmbH, Hamburg Germany) equipped with a Perkin Elmer Y Panel 4343 CT detector and 190 kV nano focus transmission tube. Exposure times were variable between 0.5 Hz– 3 Hz, depending on the sample. Long exposure times were used for high-quality scans and short exposure times for quick scans. Scans were performed either continuously or in a stop-and-go motion, for high-quality scans, with 360° rotation of the sample around a fixed position. Depending on the sample 1400–5100 projections were made, with 40–60 kV and 150–175 μA.

Fluorescence imaging

For histology, brain samples were embedded in 4% agarose and sectioned into 100 μm slices using a vibratome (Mikrom HM 650 V, Thermo Scientific). Nerve and whisker samples were prepared for cryo-sectioning by embedding in 10% sucrose and 4% agarose and then left in 30% Sucrose solution until they sunk to the bottom for cryo-protection. Samples were then sectioned into 40–60 μm slices at −15°C using a Leica Frigomobil 0247/08.1996 cryo-sectioning device.

Sections were immediately mounted on gelatine-coated slides with 0.1 M PB and imaged using a Leica DM5500B fluorescence microscope (Wetzlar, Germany). For neural tracing with Carbocyanine dyes, immediate imaging after sectioning is preferred as the dye continues to diffuse through the tissue. Leaving sections for too long can result in leaking of the dye out of the cut cells leading to diffuse and non-specific labeling. After imaging, the sections can be kept in 0.1 M PB for further histological staining.

Image post-processing

MicroCT scans were reconstructed with the YXLON reconstruction software and visualised with Dragonfly software (Dragonfly 2021.3, Object Research Systems (ORS) Inc, Montreal, Canada). Reconstructed images were segmented in an extended version of the Amira software (AmiraZIBEdition 2022.17, Zuse Institute Berlin, Germany). Fluorescence images were post-processed with Fiji (ImageJ Version 2.3.0). Adobe Illustrator (Version 26.3.1) and Photoshop (Version 23.4.1) were used for the orientation and presentation of the data.

Animal sample origin and ethics

Following the 3R Principles, no animals were killed solely for the performed experiments. Instead, all samples have their origin in animal waste from other experiments or breeding facilities or were commercially bought at a local butcher. Rat Whisker pads were obtained from 5 to 6 week-old Janvier rat cadavers originating from other experiments. The experiments from which we received cadavers were carried out according to German law for animal welfare and approved by the State Office for Health and Social Affairs committee (LAGeSo) in Berlin (Animal license number: G0279/18, G0095/21). Those animals were killed accordingly to the specific animal experimentation permits; as noted above no animals were killed solely for the purpose of this study. Piglet brains were dissected from still born piglets that were collected from a local pig farm. Pig infraorbital nerve samples were dissected out from adult pig heads obtained at a local butcher.

QUANTIFICATION AND STATISTICAL ANALYSIS

Absorption and fluorescence spectra are presented as means of triple measurements stemming from the same sample. Data for linear regressions are single measurements. The software OriginLab was used to analyze and plot the data.